

# 1 Statistics of counter-streaming solar wind suprathermal 2 electrons at solar minimum: STEREO observations

3 B. Lavraud,<sup>1,2</sup> A. Opitz,<sup>1,2</sup> J. T. Gosling,<sup>3</sup> A. P. Rouillard,<sup>4</sup> K. Meziane,<sup>5</sup> J.-A.  
4 Sauvaud,<sup>1,2</sup> A. Fedorov,<sup>1,2</sup> I. Dandouras,<sup>1,2</sup> V. Génot,<sup>1,2</sup> C. Jacquey,<sup>1,2</sup> P.  
5 Louarn,<sup>1,2</sup> C. Mazelle,<sup>1,2</sup> E. Penou,<sup>1,2</sup> D. E. Larson,<sup>6</sup> J. G. Luhmann,<sup>6</sup> P.  
6 Schroeder,<sup>6</sup> L. Jian,<sup>7</sup> C. T. Russell,<sup>7</sup> C. Foullon,<sup>8</sup> R. M. Skoug,<sup>9</sup> J. T.  
7 Steinberg,<sup>9</sup> K. D. Simunac,<sup>10</sup> and A. B. Galvin<sup>10</sup>

8  
9  
10 <sup>1</sup> Centre d'Etude Spatiale des Rayonnements, Université de Toulouse (UPS), 9 Avenue  
du Colonel Roche, 31028 Toulouse Cedex 4, France

11 <sup>2</sup> Centre National de la Recherche Scientifique, UMR 5187, Toulouse, France

12 <sup>3</sup> Laboratory for Atmospheric and Space Physics, University of Colorado, Boulder,  
13 Colorado, USA

14 <sup>4</sup> Space Environment Physics Group, School of Physics and Astronomy, University of  
15 Southampton, UK

16 <sup>5</sup> Department of Physics, University of New Brunswick, Fredericton, Canada

17 <sup>6</sup> Space Sciences Laboratory, University of California, Berkeley, USA

18 <sup>7</sup> Institute of Geophysics and Planetary Physics, University of California, Los Angeles,  
19 USA.

20 <sup>8</sup> Centre for Fusion, Space and Astrophysics, Department of Physics, University of  
21 Warwick, Coventry, UK

22 <sup>9</sup> Space Science and Applications, Los Alamos National Laboratory, Los Alamos, New  
23 Mexico, USA

24 <sup>10</sup> University of New Hampshire, Durham, USA

25 **Abstract.** Previous work has shown that solar wind suprathermal electrons can display a  
26 number of features in terms of their anisotropy. Of importance is the occurrence of counter-  
27 streaming electron patterns, i.e., with “beams” both parallel and anti-parallel to the local  
28 magnetic field, which is believed to shed light on the heliospheric magnetic field topology. In  
29 the present study, we use STEREO data to obtain the statistical properties of counter-  
30 streaming suprathermal electrons (CSEs) in the vicinity of corotating interaction regions  
31 (CIRs) during the period March – December 2007. Because this period corresponds to a  
32 minimum of solar activity, the results are unrelated to the sampling of large-scale coronal  
33 mass ejections, which can lead to CSE owing to their closed magnetic field topology. The  
34 present study statistically confirms that CSEs are primarily the result of suprathermal electron  
35 leakage from the compressed CIR into the upstream regions with the combined occurrence of  
36 halo depletion at 90° pitch angle. The occurrence rate of CSE is found to be about 15-20% on  
37 average during the period analyzed (depending on the criteria used), but superposed epoch  
38 analysis demonstrates that CSEs are preferentially observed both before and after the passage  
39 of the stream interface (with peak occurrence rate > 35% in the trailing high speed stream), as  
40 well as both inside and outside CIRs. The results quantitatively show that CSEs are common  
41 in the solar wind during solar minimum, but yet they suggest that such distributions would be  
42 much more common if pitch angle scattering were absent. We further argue that (1) the  
43 formation of shocks contributes to the occurrence of enhanced counter-streaming sunward-  
44 directed fluxes, but does not appear to be a necessary condition, and (2) that the presence of  
45 small-scale transients with closed-field topologies likely also contributes to the occurrence of  
46 counter-streaming patterns, but only in the slow solar wind prior to CIRs.

## 47 1. Introduction

### 48 1.1. Counter-streaming suprathermal electron patterns

49 Owing to their mean-free path of order 1 AU, solar wind suprathermal electrons are essentially collision-less.  
50 They travel freely along the magnetic field while thermal electrons and ions are essentially bound to one another in  
51 the solar wind rest frame. Up to about 2 keV, solar wind electrons can be decomposed into three main populations  
52 (e.g., Feldman et al., 1975; Pilipp et al., 1987a): (1) the “core” population, extending from zero to several tens of  
53 eV and whose density, temperature and anisotropy are variable; (2) the “halo” population, a tenuous and generally

54 isotropic suprathermal population (typically above 70 eV); and (3) the “strahl”, an intense beam of suprathermal  
 55 electrons aligned to the magnetic field and directed outward from the Sun; it carries a substantial heat flux away  
 56 from the solar corona. Solar wind electron spectra near 1 AU are characterized by a clear spectral breakpoint  
 57 around 70 eV that separates the halo and strahl from the thermal electrons.

58 There often occur substantial departures from the general characteristics of solar wind electrons given above.  
 59 This is specifically true for the suprathermal populations (halo and strahl) whose properties shed light on the  
 60 heliospheric magnetic topology (e.g., Gosling et al., 1987; Gosling, 1990; Kahler and Lin, 1994). In particular,  
 61 counter-streaming, i.e., sunward-directed suprathermal electron beam-like features are frequently observed in the  
 62 solar wind.

63 (1) Strahl broadening at heliospheric distances beyond 1 AU (Hammond et al., 1996) may occur due to wave-  
 64 particle interactions and pitch angle (PA) scattering (e.g., Gary et al., 1994; Vocks et al., 2005; Saito and Gary,  
 65 2007; de Koning et al., 2007; Owens et al., 2008; and references therein). This process is also deemed to contribute  
 66 to the formation of the sunward-directed portion of the roughly isotropic halo population (Gosling et al., 2001a;  
 67 Maksimovic et al., 2005; Štverák et al., 2009), which cannot be reproduced by simple exospheric solar wind  
 68 models (Lie-Svendsen et al., 1997; Pierrard et al., 1999; Maksimovic et al., 2005).

69 (2) Counter-streaming beam patterns may occur owing to the presence of magnetic field enhancements, e.g.,  
 70 within corotating interaction regions and at their bounding shocks (CIR; cf. Pizzo (1978) and Gosling and Pizzo  
 71 (1999)), downstream along magnetic field lines from the observation point. The backscattering there likely results  
 72 from wave-particle interactions and shock heating combined with simple adiabatic mirroring and particle leakage  
 73 into the upstream regions of the CIR (Gosling et al., 1993; Steinberg et al., 2005; Skoug et al., 2006). This is  
 74 discussed in further details in Section 4.

75 (3) Another feature of suprathermal solar wind electrons are halo depletions at  $90^\circ$  PA (Gosling et al., 2001a;  
 76 2002; Skoug et al., 2006). From visual inspection, Gosling et al. (2001a) found that about 10% of the 272 eV  
 77 electron PA distributions measured by ACE at 1 AU show a significant depletion in phase space density (PSD)  
 78 centered at  $90^\circ$ . They explained such depletions as the result of adiabatic mirroring and focusing of suprathermal  
 79 electrons when a magnetic field enhancement is present farther out along the magnetic field line. The PA depletion  
 80 width at a given observation point is then related to the ratio of the maximum field strength farther out to that  
 81 measured locally (cf. Figure 1). Unlike CIR-leakage and shock-related counter-streaming electron patterns (cf.  
 82 point (2) above and Section 4 later), which lead to an enhancement in the PSD of the counter-streaming part of the  
 83 population, the apparent counter-streaming that results from such depletions of the halo population is deemed to  
 84 come from an actual decrease in PSD centered at  $90^\circ$  owing to conservation of the first adiabatic invariant.  
 85 Differentiation between the two processes is sometimes difficult because both effects can be present  
 86 simultaneously (Steinberg et al., 2005).

87 (4) Subject to less controversy, counter-streaming strahls are also observed within closed solar wind field lines  
 88 with both ends attached to the Sun, such as within interplanetary coronal mass ejections (ICMEs) (e.g., Zwickl et  
 89 al., 1983; Pilipp et al., 1987b; Gosling et al., 1987; 2002, Gosling, 1990) and newly closed field regions following  
 90 from magnetic reconnection in the solar wind at the heliospheric current sheet (HCS) (Gosling et al., 2006;  
 91 Lavraud et al., 2009).

## 92 1.2. Structure of corotating interaction regions

93 Corotating interaction regions (CIRs; cf. Figure 2) are due to the overtaking (e.g., Sarabhai, 1963; Neugebauer  
 94 and Snyder, 1966; Carovillano and Siscoe, 1969) of the slow solar wind from the vicinity of the heliospheric

95 current sheet (HCS) (Schulz, 1973) by the fast solar wind that emanates from the adjacent trailing coronal hole  
96 (e.g., Gosling and Pizzo (1999), and references therein). The HCS is typically embedded within slow and dense  
97 solar wind, forming a region generally called the heliospheric plasma sheet (in analogy to that in Earth's  
98 magnetospheric tail) (e.g., Burlaga et al., 1990; Winterhalter et al., 1994). The slow solar wind that is sunward of  
99 the HCS is what directly interacts with the trailing fast solar wind (although the HCS is often already caught up by  
100 the CIR at 1 AU). Both these winds usually have the same magnetic field polarity since they are on the same side  
101 of the HCS. The boundary between the slow and fast solar winds is termed the stream interface (SI) (Burlaga,  
102 1974; Gosling et al., 1978). As depicted in Figure 2, this interaction leads to the formation of a compression region  
103 (grey area in Figure 2) with enhanced densities and magnetic field strengths (e.g., Pizzo, 1978; Gosling and Pizzo,  
104 1999). Depending on the local plasma properties and geometry of the magnetic field and flow, forward and reverse  
105 shocks may form ahead and behind the compression region (long edges of the grey area in Figure 2). These  
106 typically form beyond 1 AU (Hundhausen, 1973). The magnetic field lines that thread the compression region  
107 extend “upstream” into both the uncompressed slow and fast solar wind. This leads to a magnetic strength profile  
108 along magnetic field lines threading a CIR that resembles that sketched in Figure 1. This topology is expected on  
109 both sides of the CIR.

110 In the present paper, we investigate the properties of solar wind suprathermal electron PA distributions using  
111 STEREO data during March 1 – December 31, 2007. Under the prevalent solar minimum conditions of this period,  
112 the processes identified in Section 1.1 as responsible for counter-streaming suprathermal electron patterns are  
113 deemed to be related primarily to the nearby presence of structures such as CIRs and shocks. Previous work on  
114 counter-streaming electrons associated with CIRs and shocks have been largely based on a few case studies  
115 (Gosling et al., 2001a, 2002; Steinberg et al., 2005; Skoug et al., 2006). The aim of the present statistical study is to  
116 (1) quantify the occurrence rate of CSE as a function of definition criteria, (2) determine the CSE occurrence rate  
117 as a function of location relative to CIRs in order to demonstrate the aforementioned relationship, and (3)  
118 investigate the potential roles of pitch angle scattering and the presence of CIR-bounding shocks.

119 In the following, we define as “counter-streaming electron” (CSE) events those PA distributions that show  
120 higher phase space densities (PSDs) in both the field-aligned and anti-field-aligned directions as compared to the  
121 perpendicular (90° PA) direction. Section 2 presents the data used in the study. In Section 3 we use an event to  
122 illustrate the occurrence of CSE patterns, and then perform statistical analyses of the dataset. We discuss the results  
123 in Section 4 and give the conclusions in Section 5.

## 124 2. Instrumentation

125 The Solar Terrestrial Relations Observatory (STEREO; Kaiser et al., 2008) mission consists of two spacecraft  
126 that slowly drift ahead (referred to as ST-A) and behind (referred to as ST-B) the Earth on similar orbits around the  
127 Sun. The mission was designed to study solar phenomena stereoscopically and to study solar wind structures in a  
128 multi-spacecraft fashion. Here we primarily use data from the two Solar Wind Electron Analyzers (SWEA)  
129 (Sauvaud et al., 2008) and MAGnetometers (MAG) (Acuña et al., 2008) from the In-situ Measurements of  
130 PArticles and CME Transients (IMPACT) instrument suite (Luhmann et al., 2008), complemented by ion data  
131 from the PLasma And Supra-Thermal Ion Composition (PLASTIC) instruments (Galvin et al., 2008).

132 Identical instruments are present onboard each of the two STEREO spacecraft. The spacecraft are non-spinning  
133 due to the solar imaging requirements of the mission. The SWEA electron instruments are top-hat electrostatic  
134 analyzers with an additional deflection system (from setting a finite potential on two curved plates at its entrance)  
135 that allows measurement of incoming particles up to angles of  $\pm \sim 65^\circ$  from the regular top-hat entrance (which

136 looks in the plane perpendicular to the Sun-spacecraft direction), in the energy range [ $\sim 0, 2$ ] keV. The SWEA  
137 instruments thus measure most of the electron distribution function ( $\sim 80\%$  of the unit sphere) apart from two cones  
138 centered in the sunward and anti-sunward directions. When the magnetic field lies in these cones, pitch angle  
139 coverage is limited. Such data are not used for statistical analyses as explained in section 3.2.1.

140 The data from the normal telemetry mode used here consist of 3D distribution functions with 16 energy bins and  
141 a resolution of  $\sim 22.5^\circ$  in azimuth and  $\sim 21.7^\circ$  in polar angles. They are obtained from 2 second measurement  
142 intervals every 30 seconds. The primary data used here are PA distributions for the energy bin centered at  $\sim 250$  eV.  
143 This energy is used here as characteristic of the suprathermal population and well above the energy where  
144 significant field-aligned anisotropies in the core distribution can affect the suprathermal PA distribution (e.g.,  
145 Phillips et al., 1989; Phillips and Gosling, 1990), consistent with previous studies (cf. introduction). PA  
146 distributions have been transformed to the solar wind frame using ion flow measurements.

### 147 3. Observations

#### 148 3.1. Event illustration

149 Figure 3 shows solar wind ion, electron and magnetic field data from ST-A (cf. caption for details) for a 3-day  
150 interval starting August 6, 2007. This interval provides an illustration of a typical CIR crossing during the  
151 STEREO era under study.

152 The beginning of the interval shows the period prior to the CIR. The solar wind speed and magnetic field  
153 strength were low and the strahl was first observed anti-field-aligned at PA  $180^\circ$  (panel (c)). The HCS, where the  
154 magnetic field switched polarity from toward to away from the Sun, was crossed at about 4:30 UT on August 6.  
155 After the HCS, the strahl thus became field-aligned (PA  $0^\circ$ ) for the remainder of the interval displayed. Note that  
156 the magnetic signature of the HCS becomes evident when a zoom-in with an adapted y-axis scale is performed (not  
157 shown). After the HCS, ST-A still observed typical slow solar wind until about 3 UT on August 7 when all  
158 parameters intensified, marking the entrance into the compression region. The SI was observed inside the  
159 compressed region at 07:10 UT when the ion density dropped and the temperature increased, together with a jump  
160 in solar wind speed. This boundary clearly separated two very different plasma regimes. After the SI, ST-A stayed  
161 in the compression region for a while before definitely entering the pristine high-speed solar wind stream at  $\sim 14$   
162 UT.

163 There were no forward or reverse shocks bounding this CIR (cf. shock list compiled by L. Jian:  
164 [http://ssc.igpp.ucla.edu/forms/stereo/stereo\\_level\\_3.html](http://ssc.igpp.ucla.edu/forms/stereo/stereo_level_3.html)), although steep magnetic field gradients can be observed  
165 on occasions (e.g.,  $\sim 4$  UT and  $\sim 20$  UT on August 7, and  $\sim 6$  UT on August 8). Although shocks do develop on  
166 occasion at 1 AU on the edges of CIRs, this event was chosen specifically because it lacks the presence of  
167 bounding shocks. Despite this absence of shocks, suprathermal electron phase space densities (PSDs) are strongly  
168 enhanced inside the compression region at all PAs. This provides a source of enhanced PSD for subsequent  
169 leakage, as discussed in Section 4.

170 CSEs are observed primarily on four occasions in the vicinity of this CIR (thick black arrows in panel (c)). The  
171 first occurrence is around  $\sim 0$  UT on August 7. This corresponds to a period prior to entry into the compression  
172 region, and thus prior to the SI. The second to fourth occurrences are around 12 UT on August 7, and around 2 and  
173 9 UT on August 8. Those intervals are inside the compression region: CSE patterns are thus not confined to regions  
174 outside CIRs. The last period of CSE pattern is observed outside the CIR between 14 and 18 UT on August 8.

175 After about 18 UT on August 8, the CSE pattern disappears. This disappearance corresponds to a decrease of  
 176 PSD in the counter-streaming direction at  $180^\circ$ , as compared to the CSE around 9 UT. The enhanced PSDs  
 177 measured in the counter-streaming direction (at  $180^\circ$ ) around 9 UT are thus presumably due to leakage of electrons  
 178 from stronger field regions of the CIR, since those are absent at larger distances away from the CIR (after 18UT).  
 179 In addition to enhanced PSD values at  $180^\circ$ , the PSD values are clearly depressed at  $90^\circ$  around 9 UT as compared  
 180 to values observed at  $90^\circ$  after 18 UT on August 8. This confirms that leakage of enhanced counter-streaming  
 181 PSDs from CIRs (Gosling et al., 1993) and the process of  $90^\circ$  halo depletion (Gosling et al., 2001a) both conspire  
 182 to create strong CSE patterns in the PA spectrograms, as suggested by Steinberg et al. (2005).

### 183 3.2. Statistical analyses of CSE

#### 184 3.2.1. Data treatment and analysis

185 We utilized all STEREO data from the period March 1 – December 31, 2007. We used 10 minute averages of  
 186 the electron PA distributions and magnetic field calculated in the following manner. Individual PA distributions are  
 187 calculated using 2s electron distribution functions (i.e., 96 look directions: 16 azimuth and 6 polar angles) and the  
 188 average magnetic field during that 2s interval. Individual PA distributions used here are made of 18 bins ( $10^\circ$  each)  
 189 from a re-sampling of the 96 PAs of each original look direction. Individual 2s electron distribution functions are  
 190 telemetered only every 30s. Twenty consecutive PA distributions are thus used to create the 10 minute averages.  
 191 Therefore, only magnetic field changes at scales shorter than 2s during any sample may affect the resulting  
 192 averaged PA distribution. For the electron data such averaging is needed because the count rate at  $\sim 250$  eV, in the  
 193 large depletions for individual distributions, is sometimes close to the 1-count level when the ambient solar wind  
 194 has a low density. The SWEA instruments do not measure in two cones ( $25^\circ$  half width) directed towards and away  
 195 from the Sun. Therefore, all data from intervals when the magnetic field had a strong radial component lead to  
 196 truncated PA distributions, with a lack of data for PAs around  $0^\circ$  and  $180^\circ$ . In our analyses we removed all such  
 197 PA distributions that did not have full PA coverage (corresponding to  $\sim 15\%$  of the original dataset).

198 For each 10 minute PA distribution, we collect the average PSD values from  $0$  to  $20^\circ$ ,  $90 \pm 10^\circ$  and  $160$  to  $180^\circ$ .  
 199 The highest value of either  $0^\circ$  or  $180^\circ$  is labeled as the strahl level; the lower corresponds to the halo level (Figure  
 200 4); note this halo level may correspond to an enhanced PSD level, compared to the true halo, if strong back-  
 201 scattering or heating occurs in association with CIRs. The PSD value at  $90^\circ$  then allows us to identify a possible  
 202 counter-streaming beam pattern and to quantify its magnitude. We remind here that we term CSE those PA  
 203 distributions for which the field-aligned and anti-field-aligned PSD are higher than at  $90^\circ$ . In the following we  
 204 consider the PSD value at  $90^\circ$  PA relative to the halo PSD value as defined above. We term this the “depletion  
 205 value”. For instance, a depletion value of 0.8 corresponds to a 20% reduction in the PSD value at  $90^\circ$  as compared  
 206 to the halo value at  $0^\circ$  or  $180^\circ$  as the case may be. We also estimate the full width at half maximum (FWHM) of  
 207 the depletions, using a polynomial fitting procedure on the full PA distribution (with 18 angular bins), for depletion  
 208 values of 0.8 and lower.

209 Because our prime interest is the relationship between CSEs and CIRs, which dominantly recur during solar  
 210 minimum, we removed four known ICME intervals from the analyses (list compiled by L. Jian:  
 211 [http://ssc.igpp.ucla.edu/forms/stereo/stereo\\_level\\_3.html](http://ssc.igpp.ucla.edu/forms/stereo/stereo_level_3.html)).

#### 212 213 3.2.2. Statistical results

214 Table 1 shows the CSE occurrence rate at each spacecraft for four separate depletion value thresholds. It shows  
 215 the percentage of CSE identified for the given depletion value threshold within the entire dataset of PA

216 distributions available for analysis. The results show that stronger CSE depletions are less common, which is  
 217 expected. Overall, these occurrence rates are comparable to the value of 10% estimated by Gosling et al. (2001a)  
 218 from a visual survey of ACE data, and which were attributed to the process of 90° PA depletion described in that  
 219 paper. We note from Table 1 that the percentage of CSE events observed at ST-B is systematically greater than that  
 220 at ST-A, whatever the depletion value threshold. This is possibly related to ST-B being somewhat farther from the  
 221 Sun, where CIRs have further developed and magnetic field strengths are lower on average.

222 Figure 5(a) shows the normalized (to the peak values) occurrence distributions of the solar wind ion bulk speed  
 223 for times of CSE (solid line; depletion value threshold of 0.8) and for the whole dataset (dashed line), for ST-A and  
 224 ST-B combined. This plot shows a tendency for CSE to occur in a bimodal fashion with preference for low and  
 225 high speed solar wind, and a lower occurrence at intermediate speeds (400-500 km/s). The distribution of solar  
 226 wind speeds for all data shows a predominance of slow solar wind with a monotonic gradual decrease towards fast  
 227 wind.

228 Figure 5(b) shows the occurrence distributions of the magnetic field strength, normalized to the peak  
 229 occurrence, for ST-A and ST-B combined. The solid line displays the occurrence distribution of magnetic field  
 230 strength for times of CSE (for a depletion value threshold of 0.8) and the dashed line shows that for the whole  
 231 dataset. Figure 5(b) shows that the magnetic field magnitude is not significantly lower, on average, for times of  
 232 CSE (solid lines) than for all data (dashed lines).

233 Figure 6 shows a scatter plot of the full width at half maximum (FWHM, from a polynomial fitting procedure)  
 234 of the CSE PA distributions as a function of the depletion value, for ST-A and ST-B combined. It shows an  
 235 increase in the width of the depletion for decreasing depletion value.

236 Note that the trends observed in Figures 5 and 6 are essentially similar if plotted for each spacecraft separately  
 237 (not shown).

238

### 239 *3.2.3. Superposed epoch analysis*

240 Table 2 gives times of SIs associated with CIRs during the period of interest for both ST-A and ST-B. This list  
 241 was built from a visual examination of ion and magnetic field data. The selection of the SI times was based on the  
 242 expectation of a density decrease, a temperature increase, a bulk speed increase, and a nearby maximum in  
 243 magnetic field strength (Burlaga, 1974; Gosling et al., 1978). For an SI to be in the list, we further required that  
 244 either one of the two spacecraft observed a speed enhancement larger than 200 km/s over the inferred CIR, from  
 245 the pristine slow wind to the fast wind. We estimate possible errors on these times to be of the order of a few hours.  
 246 Such errors do not affect the results described later in major ways, as verified by separately using the SI list  
 247 compiled by L. Jian ([http://www.ssc.igpp.ucla.edu/forms/stereo/stereo\\_level\\_3.html](http://www.ssc.igpp.ucla.edu/forms/stereo/stereo_level_3.html)), which only extends as of the  
 248 time of writing until October 2007.

249 All usable data points were assigned a time relative to the closest stream interface from Table 2 for each  
 250 spacecraft independently. Figure 7 shows the normalized (to peak value) CSE occurrence (solid line) as a function  
 251 of epoch relative to stream interfaces (epoch zero). The dashed line shows the normalized (to peak value)  
 252 occurrence for all data, i.e., with and without CSE. The dotted line shows the CSE occurrence relative to the total  
 253 occurrence of data (i.e., solid curve normalized to dashed curve). Note that the temporal separations between SIs in  
 254 Table 2 are widespread (from a couple days to more than 15 days). The total number of data points (dashed lines)  
 255 thus falls off gradually on each side of zero epoch, and it does so in an irregular manner owing to the presence of  
 256 data gaps and unused data (for example because of poor PA coverage or the presence of an ICME).

257 Figure 7(a) shows the results for a depletion value of 0.8, while Figure 7(b) shows those for a depletion value of  
 258 0.6. Comparison of Figures 7(a) and 7(b) illustrates that the global features do not depend on the depletion value.  
 259 This fact is true for other depletion values (not shown). Results shown in later figures are also similar whatever the  
 260 depletion value used (though with varying statistics). The plots displayed from now on are thus only for a depletion  
 261 value of 0.8.

262 Figure 7 demonstrates that CSEs often occur near (both before and after) the stream interfaces. There is a strong  
 263 dip in CSE occurrence right at the stream interface, and the occurrence falls off at some distance each side of the  
 264 interface. We also note the presence of two peaks in the pre-SI period around -1 and -2.5 days.

265 Figure 8 shows the superposed epoch results for various plasma parameters (cf. caption). Figure 8(a) shows that,  
 266 on average, the strahl intensity peaked around the SI, and the strahl intensity was statistically similar between times  
 267 of CSE and for all data. Figure 8(b) shows the general behavior expected for CIRs, with a peak in magnetic field  
 268 strength at the SI. The remainder of Figure 8 displays the expected velocity increase, as well as the temperature  
 269 increase while a density decrease across the SI from the slow to fast solar wind.

270 Figure 9 presents the occurrence distributions of the ratio of the local magnetic field strength to that at the  
 271 nearby SI for times of CSE (solid lines) and for all data (dashed lines). For this analysis, the magnetic field from  
 272 the nearby SI (Table 2) is determined as the strongest magnetic field in a  $\pm 2$  hour window around the closest SI for  
 273 any given data sample. Interestingly, it appears that during times of CSE the distribution is not statistically  
 274 different from that for all data.

## 275 4. Discussion

### 276 4.1. Role of compression, heating and leakage

277 Figure 5(a) shows that CSE patterns occur more frequently during high-speed solar wind since the background  
 278 dataset is dominated by slow solar wind. The distribution presents a bi-modal behavior with preference for either  
 279 slow or high-speed solar wind. The trend of Figure 5(a) is thus consistent with the superposed epoch results of  
 280 Figure 7. CSE are preferentially observed both before and after the passage of CIRs, i.e., in the slow- and high-  
 281 speed winds but not near the SI where the solar wind speed is intermediate. This is as expected from the schematic  
 282 of Figure 2. At the SI in the region with enhanced magnetic field, and from the view-point of the mechanism of  $90^\circ$   
 283 PA depletion proposed by Gosling et al. (2001a), there is no depletion, and thus no counter-streaming pattern  
 284 related to it, because electrons mirror there and fill in the range of PA centered at  $90^\circ$  PA.

285 Early work on the topic of CSEs in the vicinity of CIRs primarily related their occurrence to the presence of  
 286 bounding shocks (Gosling et al., 1993). The ability of shocks to accelerate (heat) particles to suprathermal energy  
 287 implied that such CSE patterns should primarily be observed well beyond rather than at 1 AU, because co-rotating  
 288 shocks most often form after the CIR has passed 1 AU. However, Steinberg et al. (2005) noted that enhanced  
 289 sunward-directed electron fluxes are frequently observed at 1 AU as well, despite the lack of shocks locally (see  
 290 also Gosling et al., 1978). From these studies it was realized that (1) the presence of CSEs in the pristine solar wind  
 291 on either side of the CIR may owe to magnetic connection to shocks that have formed farther out in the  
 292 heliosphere, and (2) that heating also occurs at the bounding pressure waves even when shocks have not yet  
 293 developed at 1 AU.

294 Although no shocks bound the CIR illustrated in Figure 3, either forward or reverse, CSEs are observed on both  
 295 sides of the SI in the slow and fast winds (e.g., first and last thick arrows) and suprathermal electron PSDs are  
 296 enhanced within the CIR. The latter is confirmed statistically for the strahl in Figure 8a. The compression that

297 results from stream interactions has early been studied through hydrodynamic and magneto-hydrodynamic  
 298 modeling (Carovillano and Siscoe, 1969; Pizzo, 1978; Gosling et al., 1978). These works illustrate the fact that  
 299 simple adiabatic compression leads to enhanced densities and temperatures in the compression region before  
 300 shocks actually form. However, enhanced density and temperature does not correspond to enhanced suprathermal  
 301 PSDs at all PAs. Simple adiabatic compression of the populations that flow into the CIR from the upstream regions  
 302 (PA from  $0^\circ$  to  $90^\circ$  only for the event of Figure 3) in principle (Liouville's theorem) only leads to enhanced PSDs  
 303 in the perpendicular direction. In Figure 3, for example, the enhancement in PSD at  $0^\circ$  PA observed at  $\sim 20$  UT on  
 304 August 7 (i.e., with upstream around 21 UT and downstream beforehand at 18 UT), which is associated with a  
 305 pressure wave at the rear of the CIR, can only be explained by non-adiabatic heating processes, despite the lack of  
 306 a fully steepened shock. We thus concur with Steinberg et al. (2005) that additional non-adiabatic heating (such as  
 307 through electro-magnetic turbulence) is required at such pressure waves. Fully developed shocks do not constitute  
 308 a necessary ingredient for enhanced suprathermal electron PSDs within CIRs.

309 The sunward-directed (i.e.,  $90 - 180^\circ$  PA in Figure 3) part of the PA distributions, which also shows  
 310 anomalously enhanced PSDs inside the CIR, is likely explained by the combination of mirroring (towards the  
 311 enhanced magnetic field at the SI) and PA scattering of the enhanced strahl PSDs created through heating as  
 312 described above (PA scattering is further discussed in Section 4.3). The creation of this sunward-directed  
 313 population inside the CIRs, following the sequential heating and mirroring/scattering of the pristine anti-sunward-  
 314 directed halo and strahl, provides a source of enhanced suprathermal electrons directed sunward and which may  
 315 easily leak out towards upstream regions. The leaking particles then focus along the magnetic field as they exit into  
 316 a lower magnetic field so as to create a CSE pattern. The notion of leakage here is not limited to leakage into the  
 317 pristine regions outside the CIRs. As the event of Figure 3 demonstrates, CSEs may form even inside the CIRs as  
 318 long as the local magnetic field strength is lower than farther out along the field lines (Gosling et al., 2001a).

#### 319 **4.2. Role of pitch angle scattering**

320 Theoretically, the scenario proposed by Gosling et al. (2001a) for the formation of PSD depletions at  $90^\circ$  PA  
 321 (Figure 1) ought to lead to complete suprathermal electron depletions within the cone defined by the conservation  
 322 of the first adiabatic invariant and centered at  $90^\circ$  PA. However, the depletions are in reality never totally devoid of  
 323 particles (cf. Figure 4). As noted by Gosling et al. (2001a), this likely owes to the continuous occurrence of wave-  
 324 particle interactions. The associated PA scattering progressively refills the depletions and gives them their typical  
 325 reversed Gaussian shape (dashed curve in Figure 4). Assuming a fixed PA scattering coefficient (in time and  
 326 space), this refilling is expected to be more efficient (or faster) for depletions with smaller angular width, thus  
 327 explaining the correlation between the depletion value and the FWHM in Figure 6.

328 Our analysis showed that the local magnetic field strength is not significantly lower for CSE as compared to that  
 329 for all data (Figure 5(b)). CIR-related CSEs are expected to occur for lower magnetic fields, on average, since they  
 330 are typically observed in the uncompressed upstream regions. For the  $90^\circ$  PA depletion mechanism, it is the ratio  
 331 of the local to maximum (farther out along the field line) magnetic field strengths that determines the width of  
 332 depletions (Gosling et al., 2001a), and which in turn ought to control their occurrence. Figure 9 shows that the  
 333 magnetic field strength for times of CSE is generally significantly lower than at the nearby SI where the PA  
 334 distributions are expected to loose their counter-streaming shape (due to local mirroring). However, all other data  
 335 that do not present a CSE character (dashed curve), in the sense of a lower PSD at  $90^\circ$  PA, are statistically recorded  
 336 at times of similarly low magnetic field strengths when compared to the nearby SI maximum magnetic field  
 337 strength. In other words, the local magnetic field strength is often significantly lower than at the nearby SI to which

338 it is likely connected, yet no CSE pattern resulting from  $90^\circ$  PA depletion is observed. A likely explanation here as  
 339 well is the continuous occurrence of wave-particle interactions in the vicinity of and within the CIR, with  
 340 associated PA scattering refilling the depletion cone.

341 Another possibility is that the Sunward-directed leaking population may sometimes be too weak in CIRs to form  
 342 CSEs in the upstream regions. Statistically, PSD values are much higher inside the CIR than outside (Figure 8a).  
 343 This is true for the sunward-directed suprathermal population, indicating that there usually exists a significant seed  
 344 population for leakage. This is observed in Figure 3c, for instance, where we further note that enhanced Sunward-  
 345 directed electron PSDs are measured on numerous occasions together with a lack of depletion at  $90^\circ$  PA (i.e., times  
 346 in between the black arrows).

347 At some distance from the SI the magnetic topology of Figure 2 implies magnetic connection to a CIR/SI farther  
 348 out in the heliosphere, where the field strength within the CIR usually should be lower than at 1 AU. The  
 349 amplitude of the ratio displayed in Figure 9 would in principle need to be scaled accordingly. However, we believe  
 350 that scaling this ratio to the actual magnetic field strength farther out (and which is unknown) is statistically  
 351 unlikely to alter the fact that the two distributions in Figure 9 are similar.

352 The facts (1) that  $90^\circ$  PA depletions are never totally devoid of particles and (2) that CSEs are not observed as  
 353 often as one would expect from simple magnetic field ratio arguments in the vicinity of CIRs, both suggest strong  
 354 and continuous PA scattering in the vicinity of CIRs. This inferred strong PA scattering is further necessary in the  
 355 scenario proposed in section 4.1, where we suggest that the enhanced sunward-directed portion of the suprathermal  
 356 electron distributions within the CIR stems from the combination of mirroring and PA scattering of the enhanced  
 357 (compressed and heated) anti-sunward-directed strahl. Future work ought to study the presence of appropriate  
 358 waves in the vicinity of CIRs and their relation with the observation of CSEs (e.g., Horbury and Schmidt, 1999).

### 359 **4.3. Role of the bounding shocks**

360 Compression and heating occur within CIRs even in the absence of bounding shocks. This process, together  
 361 with a necessary PA scattering process, constitutes the means to produce enhanced sunward-directed PSDs. Here  
 362 “enhanced” means PSDs that are larger than the (also) sunward-directed halo PSDs observed a good distance away  
 363 from the CIR, when no CSE pattern is observed (e.g., at the very end of the interval shown in Figure 3). However,  
 364 as shown by Steinberg et al. (2005) and found in the STEREO data as well (not shown), the counter-streaming  
 365 sunward-directed PSDs outside the CIR-bounding shocks sometimes exceed those observed just inside  
 366 (downstream), which is deemed to be the source population. In a future work, we will show how the presence of  
 367 shocks may indeed permit a further increase in the CSE population PSDs by means of shock reflection.

368 The occurrence of CSE appears to be strongly related to the presence of CIRs and shocks during solar  
 369 minimum. The fact that their presence is a key ingredient, i.e., in order to provide enhanced PSDs in the sunward  
 370 direction, is a currently debated theme (cf. introduction). An alternate, or complementary, mechanism is the sole  
 371 occurrence of backscattering owing to wave-particle interactions (cf. introduction). As noted by Maksimovic et al.  
 372 (2005), CIR- and shock-related CSE should be limited to regions of the solar ecliptic where CIRs typically form. It  
 373 would be of interest in the future, using for instance data from the Ulysses spacecraft, to determine whether CSEs  
 374 occur as often (as a function of their magnitude) at higher heliospheric latitudes, since the scenario depicted here  
 375 would seem to preclude it if the field lines do not wander substantially in latitude (cf. Gosling et al. (2001b)).

### 376 **4.4. Role of small-scale transients in the slow wind**

377 In the context of the present study, it is necessary to note that a non-negligible fraction of CSE patterns observed  
378 prior to CIRs likely comes from the passage of small-scale transients with closed magnetic field topologies.  
379 Indeed, recent studies have shown that transients with CSE patterns are often observed in the slow solar wind  
380 (Kilpua et al., 2009; Rouillard et al., 2009a; 2009b; 2009c) ahead of CIRs, while not in their trailing part,  
381 compatible with their inferred streamer belt origin (Wang et al., 2000; Zurbuchen et al., 2001; Crooker et al.,  
382 2004). The determination of their exact contribution to the occurrence rate of CSEs in the slow wind prior to CIRs  
383 is a topic for future studies.

## 384 5. Conclusions

385 We have studied the properties of counter-streaming 250 eV suprathermal electron (CSE) patterns through  
386 statistical analyses of the STEREO PA distributions during the solar minimum period March 1 – December 31,  
387 2007. Our purpose was to (1) quantify the occurrence rate of CSE, (2) determine the CSE occurrence rate as a  
388 function of location relative to CIRs, and (3) investigate the potential roles of pitch angle scattering and of the  
389 presence of CIR-bounding shocks. The primary results are as follows.

390 (1) CSE occurrence rates are of the order of 15 – 20% around 1 AU, compatible with previous studies. The rates  
391 of course depend on the definition criteria. There is a clear tendency to observe more CSE at ST-B, which is farther  
392 from the Sun.

393 (2) CSEs occur for magnetic field strengths that are significantly lower than at the nearby stream interface (SI).  
394 However, CSEs are not observed as frequently as one would expect based on the assumption that the ratio of the  
395 local magnetic strength to that at the nearby SI is the only ingredient needed for their appearance.

396 (3) Larger CSE 90° PA depletion values correspond to wider depletions in pitch angles. The depletions are  
397 never totally devoid of electrons.

398 (4) CSEs with enhancements in suprathermal electron PSDs are frequently observed on both sides of CIRs, even  
399 in the absence of bounding shocks. Enhanced PSDs in the sunward direction are observed even in the absence of  
400 CSE: the absence of CSE is not typically the result of a lack of seed population (leaking from the CIR).

401 (5) As demonstrated with the event of Figure 3, CSEs may form even inside CIRs as long as the local magnetic  
402 field strength is lower than farther out along the field lines.

403 (6) CSEs are overall more frequent in the high-speed solar wind, with a bi-modal shape favoring both slow and  
404 fast wind.

405 (7) Consistent with the latter, superposed epoch analyses demonstrate that CSE occur in both the slow solar  
406 wind prior to the SI, as well as in the high-speed solar wind after the SI. There is a significant minimum occurrence  
407 at the SI itself. CSE occurrence rate peaks above 35% on average in the trailing part of CIRs.

408 Results (1), (2) and (3) above are suggestive of frequent, almost total, refilling of the expected depletions at 90°  
409 PA by wave-particle interactions and associated PA scattering. PA scattering is thus expected to be particularly  
410 strong in the CIR region. Consistently, scattering inside the CIR is required in our scenario in order to create the  
411 sunward-directed portion of the PA distribution that constitutes the source (through leakage) of the sunward  
412 directed beam in the CSE patterns observed upstream of CIRs. Non-adiabatic heating is required, in addition to  
413 scattering, to explain the enhanced PSDs inside CIRs and in the CSEs. This required additional  
414 heating/acceleration occurs whether fully developed bounding shocks are present or not (results (4) and (5)).

415 Results (6) and (7) are consistent with the expected properties and magnetic topology in the vicinity of CIRs, as  
416 sketched in Figures 1 and 2. CSEs are deemed to result primarily from leakage of enhanced backscattered  
417 suprathermal electrons from the CIRs, together with the process of 90° PA depletion owing to mirroring and

418 focusing effects (Gosling et al., 2001a; 2002; Steinberg et al., 2005; Skoug et al., 2006). CSE events unrelated to  
 419 closed magnetic field topologies are thus common in the solar wind during solar minimum, in particular in the  
 420 high-speed trailing part of CIRs. It should be noted, however, that small-scale transients with closed magnetic  
 421 topology likely also contribute to the detection of CSEs in the interval studied, but only in the slow solar wind prior  
 422 to the SI.

423 Because suprathermal electrons are widely used tracers of heliospheric magnetic topology and energetic  
 424 phenomena, future work ought to focus on characterizing the non-adiabatic heating mechanism that occurs within  
 425 CIRs (as well as at the bounding shocks), as well as the origin and implications of pitch-angle scattering.

426

427

428 **Acknowledgments.** The authors thank the entire IMPACT and PLASTIC teams for their efforts in the development of the  
 429 instruments and in the generation of the datasets. We are grateful for the use the AMDA tool at CDPP (<http://cdpp-amda.cesr.fr/>)  
 430 which allowed easy search and visualization of CIR crossings. The authors also thank the reviewers for their constructive  
 431 comments.

432

433

## 434 References

435

436 Acuña, M. H., Curtis, D., Scheifele, J. L., Russell, C. T., Schroeder, P., Szabo, A., and Luhmann, J. G.: The STEREO/IMPACT  
 437 magnetic field experiment, *Space Sci. Rev.*, 136, No. 1-4, 203-226, 2008.

438 Burlaga, L. F.: Interplanetary stream interfaces, *J. Geophys. Res.*, 79, No. 25, 3717–3725, 1974.

439 Burlaga, L. F., Mish, W. H., and Whang, Y. C.: Coalescence of recurrent streams of different sizes and amplitudes, *J. Geophys.*  
 440 *Res.*, 95, No. A4, 4247–4255, 1990.

441 Carovillano, R. L., and Siscoe, G. L.: Corotating structure in the solar wind, *Sol. Phys.*, 8, No. 2, 401, 1969.

442 Crooker, N. U., Huang, C.-L., Lamassa, S. M., Larson, D. E., Kahler, S. W., and Spence, H. E.: Heliospheric plasma sheets, *J.*  
 443 *Geophys. Res.*, 109, A03107, doi:10.1029/2003JA010170, 2004.

444 de Koning, C. A., Gosling, J. T., Skoug, R. M., and Steinberg, J. T.: Energy dependence of electron pitch angle distribution  
 445 widths in solar bursts, *J. Geophys. Res.*, 112, A04101, doi:10.1029/2006JA011971, 2007.

446 Feldman, W. C., Asbridge, J. R., Bame, S. J., Montgomery, M. D., and Gary, S. P.: Solar wind electrons, *J. Geophys. Res.*,  
 447 80(31), 4181–4196, 1975.

448 Galvin, A. B., et al.: The plasma and suprathermal ion composition (PLASTIC) investigation on the STEREO observatories,  
 449 *Space Sci. Rev.*, 136, No. 1-4, 437-486, 2008.

450 Gary, S. P., Scime, E. E., Phillips, J. L., and Feldman, W. C.: The whistler heat flux instability: Threshold conditions in the solar  
 451 wind, *J. Geophys. Res.*, 99, 23391, 1994.

452 Gosling, J. T., Asbridge, J. R., Bame, S. J., and Feldman, W. C.: Solar wind stream interfaces, *J. Geophys. Res.*, 83, No. A4,  
 453 1401–1412, 1978.

454 Gosling, J. T., Baker, D. N., Bame, S. J., Feldman, W. C., Zwickl, R. D., and Smith, E. J.: Bidirectional solar wind electron heat  
 455 flux events, *J. Geophys. Res.*, 92, No. A8, 8519–8535, 1987.

456 Gosling, J. T.: Coronal mass ejections and magnetic flux ropes in interplanetary space, in *Physics of Magnetic Flux Ropes*,  
 457 *Geophys. Monograph*, No. 58, edited by C. T. Russell, E. R. Priest, and L. C. Lee, AGU, p. 343-364, 1990.

458 Gosling, J. T., Bame, S. J., Feldman, W. C., McComas, D. J., Phillips, J. L., and Goldstein, B. E.: Counterstreaming  
 459 suprathermal electron events upstream of corotating shocks in the solar wind beyond ~2 AU: Ulysses, *Geophys. Res. Lett.*,  
 460 20, No. 21, 2335–2338, 1993.

461 Gosling, J. T., and Pizzo, V. J.: Formation and evolution of corotating interaction regions and their three dimensional structure,  
 462 *Space Sci. Rev.*, 89, No. 1-2, 21-52, 1999.

463 Gosling, J. T., Skoug, R. M., and Feldman, W. C.: Solar wind electron halo depletions at 90° pitch angle, *Geophys. Res. Lett.*,  
 464 28, No. 22, 4155–4158, 2001a.

465 Gosling, J. T., McComas, D. J., Skoug, R. M., and Forsyth, R. J.: Stream interaction regions at high heliographic latitudes during  
 466 Ulysses' second polar orbit, *Space Sci. Rev.*, 97, No. 1-4, 189-192, 2001b.

467 Gosling, J. T., Skoug, R. M., Feldman, W. C., and McComas, D. J.: Symmetric suprathermal electron depletions on closed field  
 468 lines in the solar wind, *Geophys. Res. Lett.*, 29, No. 12, 1573, doi:10.1029/2001GL013949, 2002.

469 Gosling, J. T., McComas, D. J., Skoug, R. M., and Smith, C. W.: Magnetic reconnection at the heliospheric current sheet and the  
 470 formation of closed magnetic field lines in the solar wind, *Geophys. Res. Lett.*, 33, L17102, doi:10.1029/2006GL027188,  
 471 2006.

472 Hammond, C. M., Feldman, W. C., McComas, D. J., Phillips, J. L., and Forsyth, R. J.: Variation of electron-strahl width in the  
 473 high-speed solar wind: Ulysses observations, *Astron. Astrophys.*, No. 316, 350-354, 1996.

474 Horbury, T. S., and Schmidt, J. M.: Development and effects of turbulence in connection with CIRs, *Space Sci. Rev.*, 89, No. 1-  
 475 2, 61-76, 1999.

476 Hundhausen, A. J.: Nonlinear model of high-speed solar wind streams, *J. Geophys. Res.*, 78, No. 10, 1528–1542, 1973.

477 Kaiser, M. L., Kucera, T. A., Davila, J. M., St. Cyr, O. C., Guhathakurta, M., and Christian, E.: The STEREO mission: An  
 478 introduction, *Space Sci. Rev.*, 136, No. 1-4, 5-16, 2008.

479 Kahler, S., and Lin, R. P.: The determination of interplanetary magnetic field polarities around sector boundaries using  $E > 2$   
 480 keV electrons, *Geophys. Res. Lett.*, 21, No. 15, 1575–1578, 1994.

- 481 Kilpua, E. K. J., Luhmann, J. G., Gosling, J., et al.: Small solar wind transients and their connection to the large-scale coronal  
 482 structure, *Solar Phys.*, 256, No. 1-2, 327-344, 2009.
- 483 Lavraud, B., Gosling, J. T., Rouillard, A. P., et al.: Observations of a complex solar wind reconnection exhaust from spacecraft  
 484 separated by over 1800 RE<sub>s</sub>, *Solar Phys.*, 256, No. 1-2, 379-392, doi:10.1007/s11207-009-9341-x, 2009.
- 485 Lie-Svendsen, Ø., Hansteen, V. H., and Leer, E.: Kinetic electrons in high-speed solar wind streams: Formation of high-energy  
 486 tails, *J. Geophys. Res.*, 102, No. A3, 4701-4718, 1997.
- 487 Luhmann, J. G., Curtis, D. W., Schroeder, P., et al.: STEREO IMPACT investigation goals, measurements, and data products  
 488 overview, *Space Sci. Rev.*, 136, No. 1-4, 117-184, 2008.
- 489 Maksimovic, M., et al.: Radial evolution of the electron distribution functions in the fast solar wind between 0.3 and 1.5 AU, *J.*  
 490 *Geophys. Res.*, 110, A09104, doi:10.1029/2005JA011119, 2005.
- 491 Neugebauer, M., and Snyder, C. W.: Mariner 2 observations of the solar wind 1. Average properties, *J. Geophys. Res.*, 71, No.  
 492 19, 4469-4484, 1966.
- 493 Owens, M. J., Crooker, N. U., and Schwadron, N. A.: Suprathermal electron evolution in a Parker spiral magnetic field, *J.*  
 494 *Geophys. Res.*, 113, A11104, doi:10.1029/2008JA013294, 2008.
- 495 Phillips, J. L., Gosling, J. T., McComas, D. J., Bame, S. J., and Gary, S. P.: Anisotropic thermal electron distributions in the  
 496 solar wind, *J. Geophys. Res.*, 94, 6563-6579, 1989.
- 497 Phillips, J. L., and Gosling, J. T.: Radial evolution of suprathermal electron distributions due to expansion and collisions, *J.*  
 498 *Geophys. Res.*, 95, 4217-4228, 1990.
- 499 Pierrard, V., Maksimovic, M., and Lemaire, J.: Electron velocity distribution functions from the solar wind to the corona, *J.*  
 500 *Geophys. Res.*, 104, No. A8, 17,021-17,032, 1999.
- 501 Pilipp, W. G., Miggenrieder, H., Montgomery, M. D., Mühlhäuser, K.-H., Rosenbauer, H., and Schwenn, R.: Characteristics of  
 502 electron velocity distribution functions in the solar wind derived from the Helios plasma experiment, *J. Geophys. Res.*, 92,  
 503 No. A2, 1075-1092, 1987a.
- 504 Pilipp, W. G., Miggenrieder, H., Montgomery, M. D., Mühlhäuser, K.-H., Rosenbauer, H., and Schwenn, R.: Unusual electron  
 505 distribution functions in the solar wind derived from the Helios plasma experiment: Double-strahl distributions and  
 506 distributions with an extremely anisotropic core, *J. Geophys. Res.*, 92, No. A2, 1093-1101, 1987b.
- 507 Pizzo, V.: A three-dimensional model of corotating streams in the solar wind, 1. Theoretical foundations, *J. Geophys. Res.*, 83,  
 508 No. A12, 5563-5572, 1978.
- 509 Rouillard, A. P., Savani, N., Davies, J. A., et al.: A multi-spacecraft analysis of a small-scale transient entrained by solar wind  
 510 streams, *Solar Phys.*, 256, No. 1-2, 307-326, doi:10.1007/s11207-009-9329-6, 2009a.
- 511 Rouillard, A. P., Lavraud, B., Davies, J. A., et al.: Intermittent release of small-scale transients in the slow solar wind: II, In-situ  
 512 evidences, *J. Geophys. Res.*, in press, 2009b.
- 513 Rouillard, A. P., Davies, J. A., Lavraud, B., et al.: Intermittent release of small-scale transients in the slow solar wind: I, Remote  
 514 sensing observations, *J. Geophys. Res.*, in press, 2009c.
- 515 Sarabhai, V.: Some consequences of nonuniformity of solar wind velocity, *J. Geophys. Res.*, 68, No. 5, 1555-1557, 1963.
- 516 Sauvaud, J.-A., Larson, D., Aoustin, C., et al.: The IMPACT Solar Wind Electron Analyzer (SWEA), *Space Sci. Rev.*, 136, No.  
 517 1-4, 227-239, 2008.
- 518 Saito, S., and Gary, S. P.: Whistler scattering of suprathermal electrons in the solar wind: Particle-in-cell simulations, *J.*  
 519 *Geophys. Res.*, 112, A06116, doi:10.1029/2006JA012216, 2007.
- 520 Schulz, M.: Interplanetary sector structure and the heliomagnetic equator, *Astrophys. Space Sci.*, 24, 371, 1973.
- 521 Skoug, R. M., Gosling, J. T., McComas, D. J., Smith, C. W., and Hu, Q.: Suprathermal electron 90° pitch angle depletions at  
 522 reverse shocks in the solar wind, *J. Geophys. Res.*, 111, A01101, doi:10.1029/2005JA011316, 2006.
- 523 Steinberg, J. T., Gosling, J. T., Skoug, R. M., and Wiens, R. C.: Suprathermal electrons in high-speed streams from coronal  
 524 holes: Counterstreaming on open field lines at 1 AU, *J. Geophys. Res.*, 110, A06103, doi:10.1029/2005JA011027, 2005.
- 525 Štverák, Š., Maksimovic, M., Trávníček, P. M., Marsch, E., Fazakerley, A. N., and Scime, E. E.: Radial evolution of nonthermal  
 526 electron populations in the low-latitude solar wind: Helios, Cluster, and Ulysses Observations, *J. Geophys. Res.*, 114,  
 527 A05104, doi:10.1029/2008JA013883, 2009.
- 528 Vocks, C., Salem, C., Lin, R. P., and Mann, G.: Electron halo and strahl formation in the solar wind by resonant interaction with  
 529 whistler waves, *Astrophys. J.*, 627, 540-549, doi:10.1086/430119, 2005.
- 530 Wang, Y.-M., Sheeley Jr., N. R., Socker, D. G., Howard, R. A., and Rich, N. B.: The dynamical nature of coronal streamers, *J.*  
 531 *Geophys. Res.*, 105, No. A11, 25,133-25,142, 2000.
- 532 Winterhalter, D., Smith, E. J., Burton, M. E., Murphy, N., and McComas, D. J.: The heliospheric plasma sheet, *J. Geophys. Res.*,  
 533 99, No. A4, 6667-6680, 1994.
- 534 Zurbuchen, T. H., Hefti, S., Fisk, L. A., Gloeckler, G., Schwadron, N. A., Smith, C. W., Ness, N. F., Skoug, R. M., McComas,  
 535 D. J., and Burlaga, L. F.: On the origin of microscale magnetic holes in the solar wind, *J. Geophys. Res.*, 106, No. A8,  
 536 16,001-16,010, 2001.
- 537 Zwickl, R. D., Asbridge, R. J., Bame, S. J., Feldman, W. C., Gosling, J. T., and Smith, E. J.: Plasma properties of driver gas  
 538 following interplanetary shocks observed by ISEE-3, Solar Wind Five, NASA Conf. Publ. CP-2280, 711-717, 1983.

543 B. Lavraud, Centre d'Etude Spatiale des Rayonnements, 9 Ave. du Colonel Roche, 31028 Toulouse Cedex 4, France  
 544 (Benoit.Lavraud@cesr.fr).

548 LAVRAUD ET AL.: SOLAR WIND COUNTER-STREAMING ELECTRONS

549  
 550  
 551  
 552  
 553  
 554  
 555  
 556

557  
558  
559**TABLES:**

Depletion value	0.8	0.7	0.6	0.5
STEREO-A rate (%)	15.5	9.7	5.5	3.1
STEREO-B rate (%)	19.7	13.4	9.1	5.9

560  
561  
562  
563  
564  
565  
566  
567

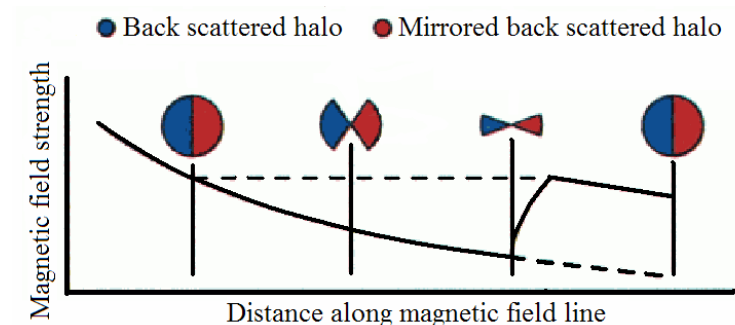
**Table 1.** Occurrence rate (in percent) of solar wind counter-streaming electron pitch angle distributions for each STEREO spacecraft during the solar minimum period March 1<sup>st</sup> – December 31<sup>st</sup>, 2007. These are given as a function of the depletion value (i.e., relative to the ambient halo value; cf. text).

ST-A: Year DOY Month Day Hour	ST-B: Year DOY Month Day Hour
2007 65 03 06 14	2007 65 03 06 16
2007 71 03 12 12	2007 71 03 12 14
2007 84 03 25 02	2007 84 03 25 08
2007 91 04 01 02	2007 91 04 01 04
2007 98 04 08 22	2007 99 04 09 10
2007 113 04 23 02	2007 113 04 23 08
2007 117 04 27 22	2007 117 04 27 16
2007 127 05 07 14	2007 127 05 07 14
2007 138 05 18 16	2007 138 05 18 08
2007 144 05 24 16	2007 144 05 24 14
2007 155 06 04 14	2007 155 06 04 00
2007 165 06 14 18	2007 165 06 14 10
2007 173 06 22 06	2007 173 06 22 06
2007 181 06 30 08	2007 180 06 29 14
2007 185 07 04 12	2007 184 07 03 14
2007 192 07 11 14	2007 191 07 10 22
2007 196 07 15 06	2007 195 07 14 12
2007 201 07 21 04	2007 201 07 20 06
2007 208 07 27 06	2007 207 07 26 14
2007 210 07 29 12	2007 210 07 29 08
2007 219 08 07 08	2007 218 08 06 12
2007 223 08 11 04	2007 222 08 10 16
2007 238 08 26 20	2007 237 08 25 00
2007 246 09 03 06	2007 244 09 01 10
2007 250 09 07 22	2007 249 09 06 14
2007 258 09 15 06	2007 257 09 14 10
2007 264 09 21 22	2007 263 09 20 02
2007 273 09 30 02	2007 271 09 28 08
2007 277 10 04 08	2007 276 10 03 02
2007 292 10 19 08	2007 290 10 17 08
2007 299 10 26 06	2007 297 10 24 20
2007 314 11 10 16	2007 314 11 10 00
2007 318 11 14 10	2007 317 11 13 08
2007 325 11 21 04	2007 324 11 20 00
2007 330 11 26 00	2007 327 11 23 22
2007 346 12 12 16	2007 343 12 09 14
2007 353 12 19 00	2007 350 12 16 12
2007 355 12 21 00	2007 352 12 18 18

568  
569  
570  
571  
572  
573  
574  
575  
576  
577  
578  
579  
580  
581  
582  
583  
584  
585

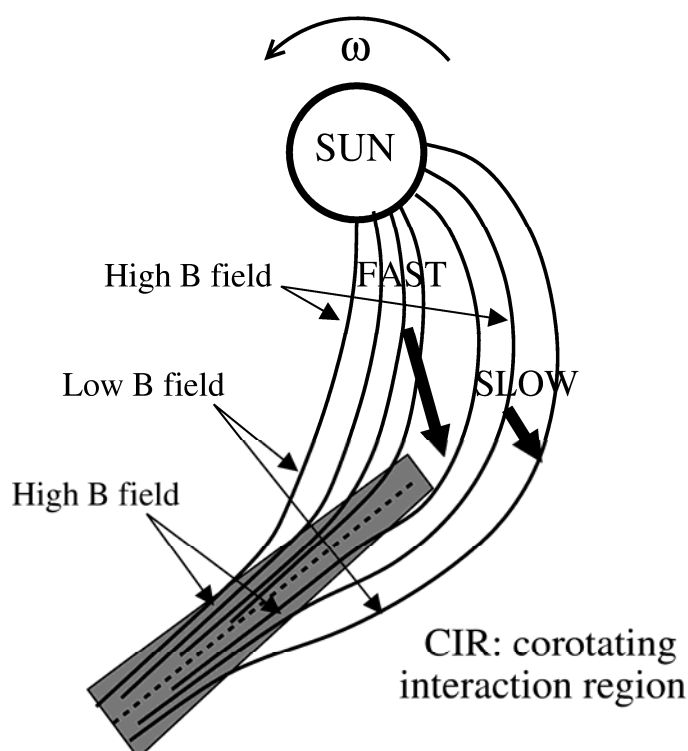
**Table 2.** List of stream interfaces associated with CIRs at each of the two STEREO spacecraft during the period March 1<sup>st</sup> – December 31<sup>st</sup>, 2007. See Figure 2 and text for SI definition.

586  
587  
588  
589



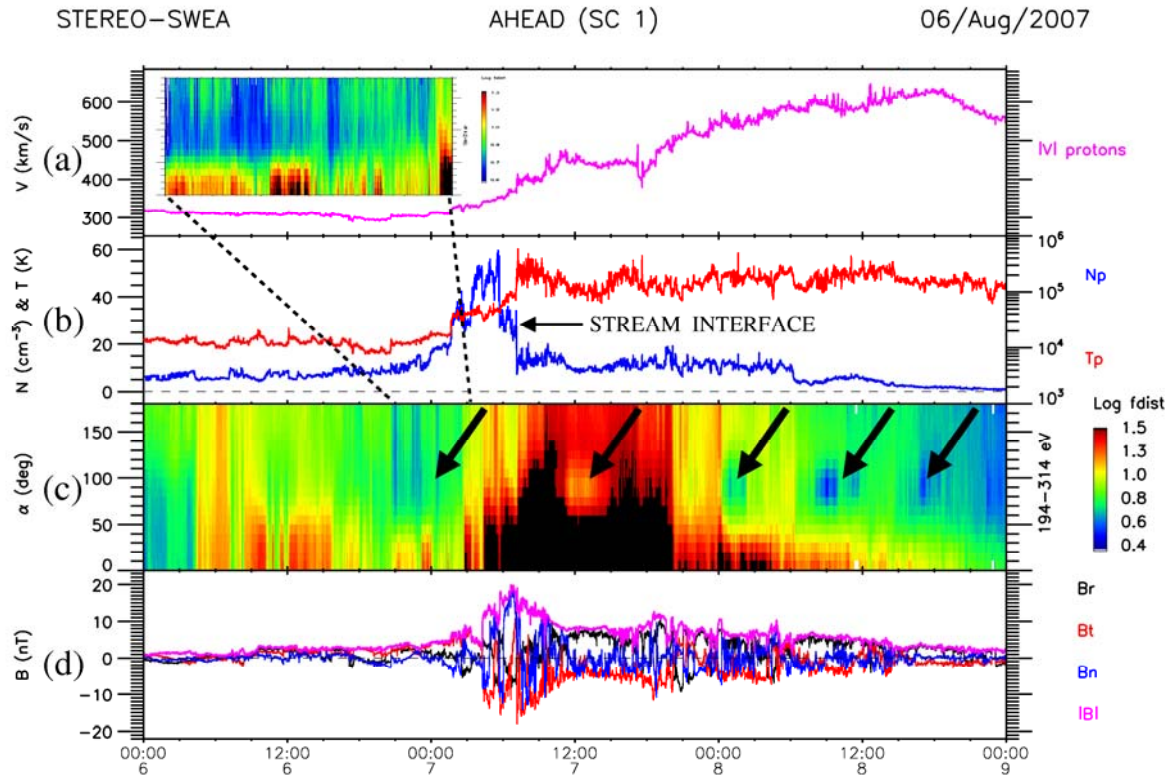
590  
591  
592  
593  
594  
595  
596  
597  
598  
599  
600

**Figure 1.** Schematic illustration of changes in suprathermal electron pitch angle distributions assuming adiabatic evolution along a magnetic field line with a non-monotonic magnetic strength decrease away from the Sun. See text for details. Adapted from Gosling et al. (2001a) and Skoug et al. (2005).

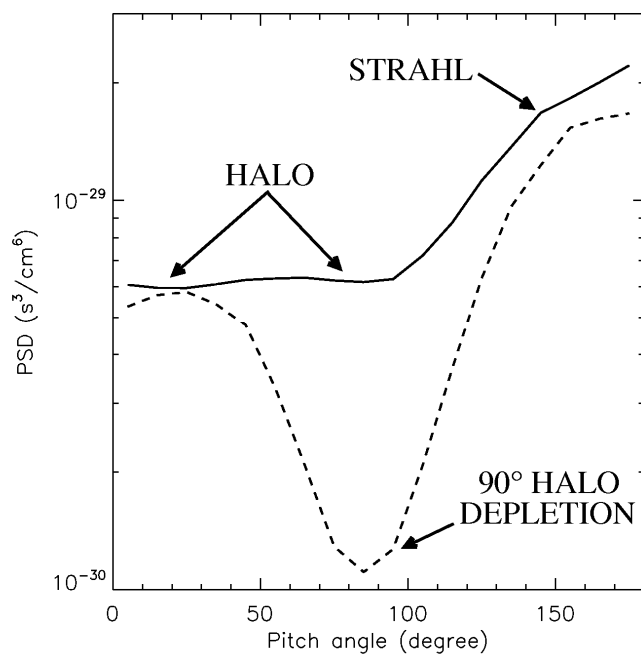


601  
602  
603  
604  
605  
606  
607  
608  
609  
610  
611  
612  
613  
614

**Figure 2.** Schematic of the structure of a corotating interaction region (CIR) in the solar wind which may lead to (1) magnetic field strength profiles, along a given field line, like that depicted in Figure 1 in both the high-speed and low-speed solar wind each side of the compression region, as well as (2) the formation of forward and reverse shocks bounding the compression region (long edges of the grey area). The stream interface (SI) is identified here as the dashed line inside the CIR.

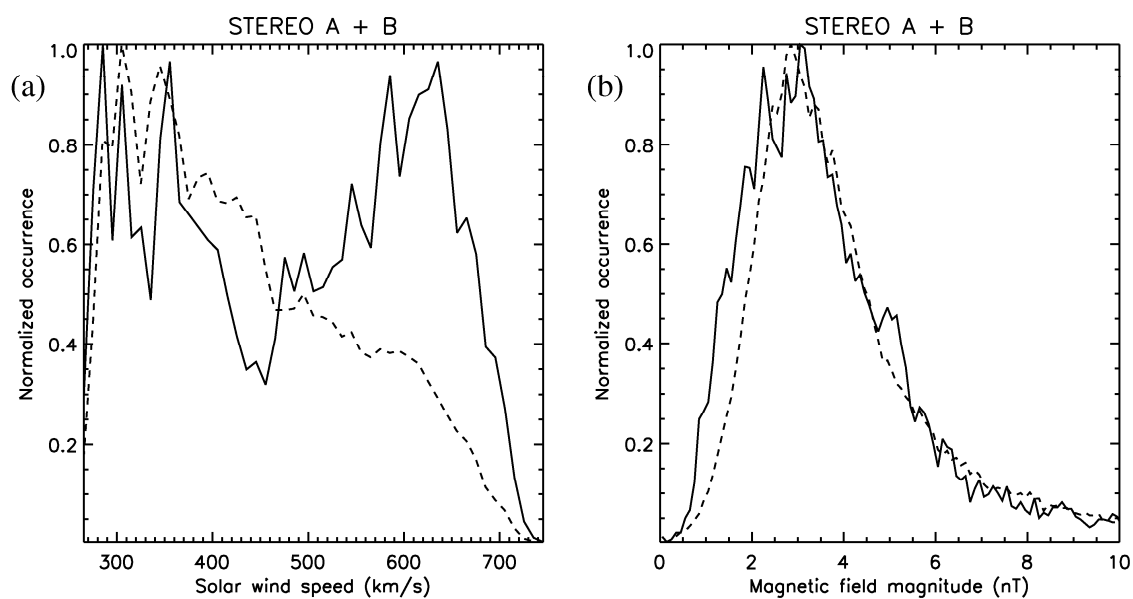
615  
616617  
618  
619  
620  
621  
622  
623  
624  
625  
626  
627  
628  
629  
630  
631  
632  
633

**Figure 3.** Ion, electron and magnetic field data from ST-A during the passage of a CIR in August 2006 (spacecraft position was  $(+1973, -5271, 45)$   $R_E$  in GSE, on August 7 2007). The panels show (a) the ion bulk speed, (b) the ion density (left y-axis) and temperature (right y-axis), (c) a pitch angle-time spectrogram for  $\sim 250$  eV suprathermal electrons, and (d) the magnetic field magnitude and components in RTN. Counter-streaming suprathermal electron patterns (CSE) are observed prior to the CIR, around the beginning of August 7 2007 (first thick black arrow), as best displayed in the zoom-in pitch angle spectrogram insert of panel (a). CSEs are also clearly observed within (second to fourth black arrow) and after the CIR (last black arrow) in the fast solar wind.



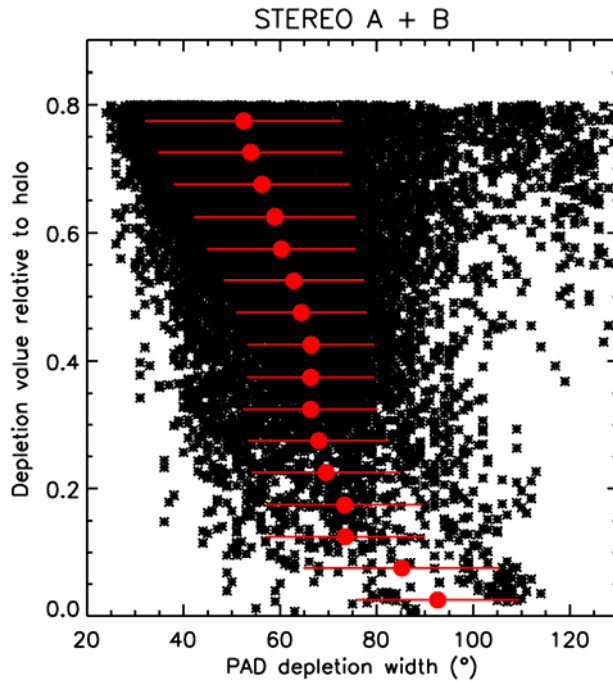
634  
635 **Figure 4.** Sample suprathermal electron PA spectra at ~250  
636 eV. Those are not from the event of Figure 3, and are merely  
637 used here to exemplify the definitions used in Section 3.2.1.

638  
639  
640  
641



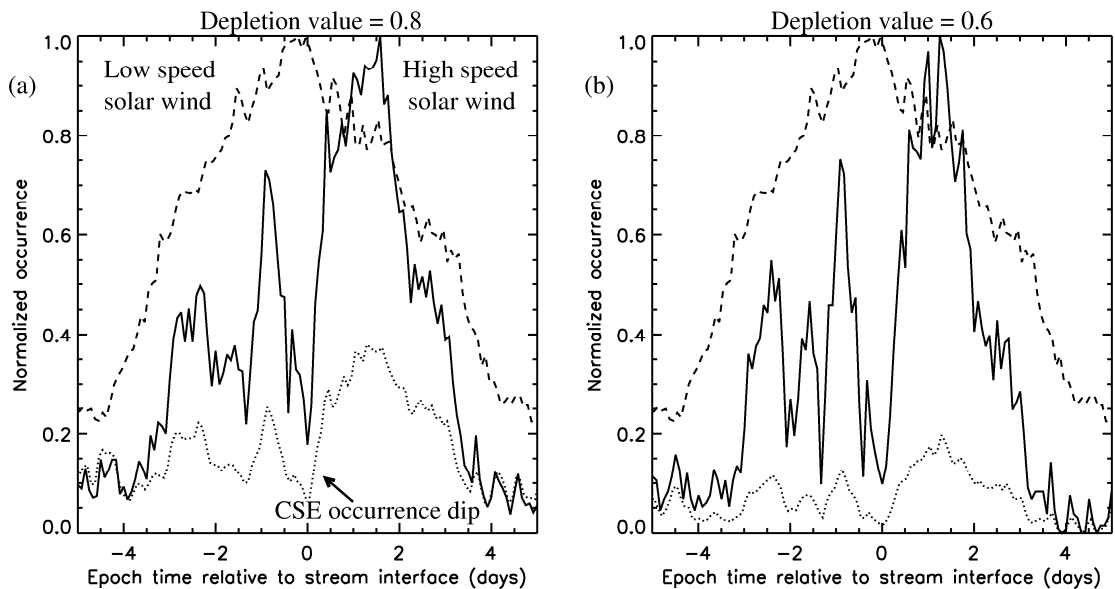
642  
643 **Figure 5.** Normalized occurrence distributions of (a) bulk solar wind speed, and (b) magnetic field magnitude, for data  
644 from ST-A and ST-B combined. The dashed lines show the distributions for the whole dataset used in the study, while the  
645 solid lines show the distribution for times of counter-streaming suprathermal electrons (CSE). The distributions are for a  
646 depletion value threshold of 0.8. Those for other depletion values are similar (not shown).

647  
648  
649



650  
 651 **Figure 6.** Scatter plot of the full width at half maximum  
 652 (FWHM) of the depletion in electron PA distributions as a  
 653 function of the depletion value (cf. Figure 3 and text for details),  
 654 for ST-A and ST-B combined. Average values of the FWHM  
 655 (red dots), with standard deviations (horizontal red lines), are  
 656 shown as a function of the depletion value (bin size of 0.5).

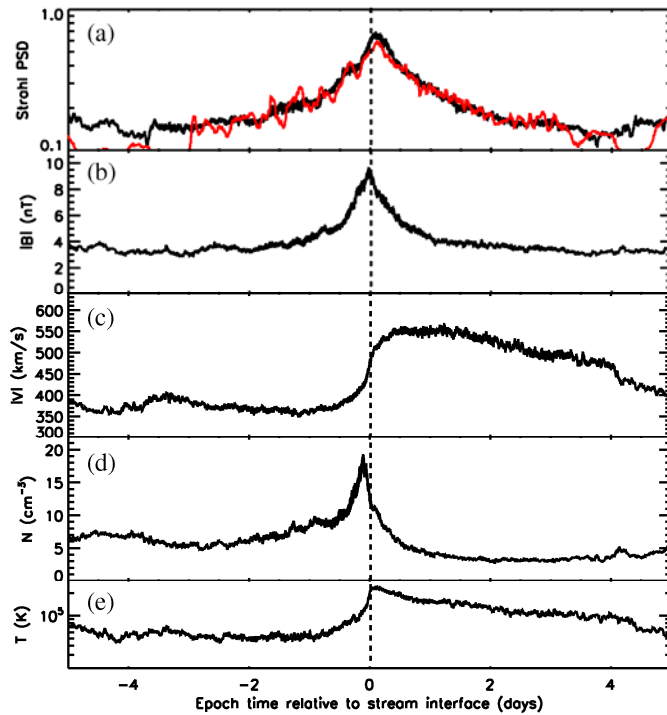
657  
 658  
 659



660  
 661 **Figure 7.** Superposed epoch analysis of the occurrence of counter-streaming suprathermal electrons (CSE; solid line) and  
 662 of all data (dashed line), relative to the time of the closest stream interface from Table 2, and normalized to the peak  
 663 value. Epoch zero thus corresponds to the times of SI crossing, with negative (positive) epoch times being the preceding  
 664 slow solar wind (following high speed wind). A two-hour interval binning has been used. The dotted lines show the CSE  
 665 occurrence normalized to that of all data (i.e., solid curve normalized to dashed curve). (a) Results for a depletion value  
 666 of 0.8. (b) Results for a depletion value of 0.6. The CSE occurrence in Figure (a) varies between ~10 and 270 counts (per  
 667 2-hour bin), giving a high statistical significance to the trends. Occurrences are about twice to three times smaller in  
 668 Figure (b) (cf. Table 1), which is still significant. See text for further details.

669  
 670

671



672

673

674

675

676

677

678

679

680

681

682

683

684

685

686

687

688

689

690

691

692

693

694

695

696

697

698

699

700

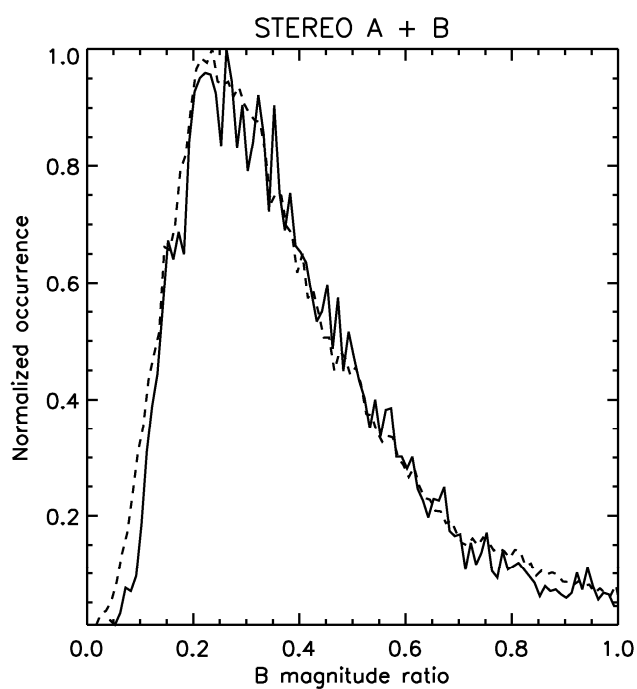
701

702

703

704

**Figure 8.** Superposed epoch results from all data relative to the times of the stream interfaces of Table 2. Results are shown for (a) the strahl phase space density (arbitrary units), (b) the magnetic field magnitude, (c) the ion bulk solar wind speed, (d) the ion density, and (e) the ion temperature. In panel (a), the results for the strahl PSD during times of CSE only is also shown in red; it illustrates the fact that the strahl during CSE intervals has a similar strength, on average, as for other times. All curves are 100-point running averages of the superposed epoch dataset (cf. text for details).



705  
706  
707  
708  
709  
710  
711  
712  
713  
714  
715

**Figure 9.** Occurrence distributions of the ratio of the local magnetic field strength to that at the nearby SI for times of CSE (solid lines) and all data (dashed lines). The magnetic field at the nearby SI (Table 2) is determined as the strongest field in a  $\pm 2$  hour interval around the SI. During times of CSE, the distribution is not statistically different from that for all data.